A&A, 709, A52 (2026)
https://doi.org/10.1051/0004-6361/202554562

Astronomy & Astrophysics

From synthetic SEDs to stellar origins: A deep learning model for physical parameter retrieval in hot subdwarf stars

Mengqi Feng[1], Zhenxin Lei[1,⋆], Bokai Kou[1], Yangyang Dong[1], Ke Hu[1], Huaping Xiao[1], and Jingkun Zhao[2]

[1] Key Laboratory of Stars and Interstellar Medium, Xiangtan University, Xiangtan 411105, PR China
[2] Key Laboratory of Optical Astronomy, National Astronomical Observatories, Chinese Academy of Sciences, Beijing 100012, China

Received 16 March 2025 / Accepted 5 March 2026

ABSTRACT

Aims. The formation mechanisms of spectrally diverse hot subdwarfs remain unclear. While existing mass distribution analyses suggest additional channels beyond helium white dwarf (He-WD) mergers contribute to He-rich subdwarf formation, these conclusions are constrained by the limited sample sizes of mass-measured He-rich objects.
Methods. We developed a deep learning model that combines a convolutional neural network (CNN) with a squeeze-and-excitation (SE) block to calculate synthetic spectral energy distributions (SEDs) for 1012 spectroscopically confirmed hot subdwarfs. By directly comparing synthetic SEDs and the observed flux density, we derived stellar parameters (mass, radius, and luminosity) for an unprecedented number of hot subdwarf stars, enabling more conclusive channel discrimination than prior studies.
Results. The mass distribution of sdB/sdOB stars confirmed the results from model predictions of binary population synthesis (BPS). A primary and secondary peak (i.e., around 0.56 and 0.4 $M_\odot$) is obviously presented in the mass distribution of He-rich hot subdwarf stars. By comparing this with the results from the predictions of the recent BPS model, we propose that the merger of two He-WDs could produce most of the observed He-rich hot subdwarf stars, but the mass transfer during the stable Roche lobe overflow phase in binary evolution should be partially conserved.

Key words. binaries: close – stars: evolution – stars: fundamental parameters

1. Introduction

Hot subdwarf stars are positioned between main-sequence (MS) and white dwarf (WD) regions in the Hertzsprung-Russell diagram (HRD) (Heber 1986). Hot subdwarf stars have very low stellar masses (e.g., 0.5 $M_\odot$) and thin envelopes ($M_{\rm env} \leq 0.02\,M_\odot$), but exhibit very high effective temperatures (e.g., $20\,000\,{\rm K} \leq T_{\rm eff} \leq 70\,000\,{\rm K}$) and large surface gravities (e.g., $5.0 \leq \log g \leq 6.5$). These blue stars have a diversity of atmospheric compositions that could present atmospheres from pure hydrogen (H) to pure helium (He). According to their spectral line features, hot subdwarfs can be classified into sdB, sdO, sdOB, He-sdB, He-sdO, and He-sdOB types (Moehler et al. 1990; Geier et al. 2017a; Lei et al. 2018). In addition, Drilling et al. (2013) designed an MK-like classification scheme by which hot subdwarf stars could be classified in a similar way as normal MS stars (also see Jeffery et al. 2021; Zou & Lei 2024). SdB stars are also referred to as extreme horizontal branch (EHB) stars due to their location at the bluest end of the horizontal branch (HB). More characteristics of hot subdwarf stars were described in recent excellent reviews of Heber (2009, 2016).

Generally, single stars with such low stellar masses as hot subdwarfs cannot evolve into core He burning or even a late stage within Hubble time. Although formation channels connected with single stars were proposed by several authors (Castellani & Castellani 1993; Miller Bertolami et al. 2008), Pelisoli et al. (2020) found that binary interactions are always required in the formation of hot subdwarf stars, including those in wide binary systems. Furthermore, most of the sdB-type hot subdwarfs were found in close binaries (Maxted et al. 2001; Napiwotzki et al. 2004; Copperwheat et al. 2011; He et al. 2025). These results indicate that binary evolution could provide natural explanations for the formation of hot subdwarfs.

Han et al. (2002, 2003) investigated the characteristics of hot subdwarfs formed through binary evolution using the binary population synthesis (BPS) method. They found that stable Roche lobe overflow (RLOF), common envelope (CE) ejection, and the merger of two helium white dwarfs (He-WDs) could produce sdB stars in long-period binaries, short-period binaries, and single sdB stars, respectively. Most of the observed characteristics for sdB stars could be satisfied by their model predictions. Zhang & Jeffery (2012) and Zhang et al. (2017) studied in detail the mergers of two He-WDs and a WD + MS star, respectively. They found that both channels could produce He-rich sdB stars such that their observed features could be satisfied. In addition, Miller Bertolami et al. (2022) proposed that the merger of carbon-oxygen WDs with He WDs could form He-rich hot subdwarfs with atmospheres strongly enriched by carbon and oxygen. Recently, Meng & Luo (2021) and Ji et al. (2024) proposed that the MS companion of massive WD could survive the type Ia supernova (SN) explosions and become intermediate He-rich hot subdwarf stars if their envelopes are ejected during the explosion. Their model predicted that the peak of mass distribution for survived stars is around 0.4 $M_\odot$, which is consistent with the results in Lei et al. (2023b). However, the birth rate of this channel would be too low compared to the number of He-rich hot subdwarf stars discovered up to now (Meng & Luo 2021).

⋆ Corresponding author: leizhenxin2060@163.com

Li et al. (2024) proposed that massive sdO/B stars could be produced from CE ejection process with an asymptotic giant branch (AGB) star. This model could explain the recently discovered sdO binary star SMSS-J1920 (Li et al. 2022), for which strong Ca H and K lines are presented in its spectrum.

With a large number of new hot subdwarf stars having been discovered using the new data release of spectroscopic surveys (Geier et al. 2017b; Kepler et al. 2019; Lei et al. 2018, 2019, 2020, 2023a; Luo et al. 2019, 2021; Schaffenroth et al. 2019; Jeffery et al. 2021), also with the help of the Gaia mission Early Data Release 3 (Gaia EDR3, Gaia Collaboration 2021), Culpan et al. (2022) compiled two catalogs for known hot subdwarf stars and their candidates, respectively (also see the serial studies, Geier et al. 2017a, 2019; Geier 2020). The catalog of known hot subdwarfs contains more than 6000 identified hot subdwarf stars, in which more than 3000 stars have atmospheric parameters and 2700 stars have radial velocities. The candidate catalog contains more than 60 000 objects, which can be used as reliable input catalogs for follow-up analysis with new observed data from spectroscopy.

Driven by the availability of large observational datasets, machine learning has been extensively applied in astronomical research, including studies of hot subdwarfs. Bu et al. (2019) combined a convolution neural network (CNN) with a support vector machine (SVM) to classify hot subdwarf stars in the dataset of Large Sky Area Multi-Fiber Spectroscopic Telescope (LAMOST, Cui et al. 2012; Zhao et al. 2012). Tan et al. (2022) also used CNN to search for hot subdwarf candidates in a larger LAMOST spectra dataset. More recently, Liu et al. (2024) applied the machine learning method to identify hot subdwarfs using photometric data, while Cheng et al. (2024) constructed a Se-ResNet+SVM model to search for hot subdwarf stars and predicted their atmospheric parameters.

Despite considerable progress having been made both in simulation and observation of hot subdwarf stars, questions remain regarding the formation channels for those stars. Some notable challenges stem from the determination of physical parameters, such as masses, radii, and luminosities. Accurate mass estimation methods include asteroseismology and Eclipse binary. However, their applications are limited by the strict requirements of observed data that only dozens of hot subdwarfs have accurate masses determined by these methods (Fontaine et al. 2012). To analyze the mass distribution of hot subdwarfs with different companion types, Schaffenroth et al. (2022) obtained masses, radii, and luminosities for 68 hot subdwarf stars by comparing observed fluxes with synthetic fluxes calculated from spectral energy distributions (SEDs). With the help of these parameters, and with the help of space-based light curves from the Transiting Exoplanet Survey Satellite (TESS, Ricker et al. 2015) and the K2 space mission (Howell et al. 2014), Schaffenroth et al. (2023) further obtained the masses of 27 companions for these hot subdwarf binaries.

Using a similar method, Lei et al. (2023b) obtained masses, radii, and luminosities for 664 single-lined hot subdwarfs with the spectra of LAMOST. Based on this large size of sample, they obtained the mass distributions for hot subdwarf stars with different spectral types, and compared them with the results from model predictions. Although the mass distribution of sdB/sdOB stars is consistent with the prevailing model of Han et al. (2002, 2003), they found that He-rich hot subdwarf stars have an obviously lower peak of mass distribution (e.g., around $0.42\,M_{\odot}$) than model predictions (e.g., $0.5-0.6\,M_{\odot}$, see Fig. 12 in Lei et al. 2023b). Based on these comparisons, they proposed that besides the two He-WDs merging channel, there should be other important formation channels for He-rich hot subdwarfs. However, only 39 He-rich stars were used in their statistical analysis, and such a small size sample would influence the final conclusions.

As a further study of Lei et al. (2023b), we constructed a deep learning architecture that integrates a CNN with a squeeze-and-excitation (SE) block to calculate the synthetic SEDs for more than 2000 known hot subdwarfs selected in Culpan et al. (2022) with the spectra of LAMOST and Sloan Digital Sky Survey (SDSS, Ahumada et al. 2020). Using these SEDs, we calculated the synthetic fluxes at stellar surface and compared them with fluxes observed on the Earth to obtain masses, radii, and luminosities for the selected hot subdwarf stars. These parameters were used in following statistical analysis to help us understand the formation of hot subdwarfs more deeply. The structure of this paper is as follows. Sample selection and methods are described in Section 2. Section 3 presents our main results. A detailed discussion for mass distribution with a large size of sample is given in Section 4. A brief summary in Section 5 closes this paper.

2. Methodology and sample selection

2.1. Deep learning model SENN

We designed a deep learning model, which integrates a CNN with a SE block (hereafter SENN), to calculate synthetic SEDs for selected hot subdwarf stars. As is shown in Fig. 1, SENN accepts normalized stellar spectra with a shape of 2984×1 as inputs, and processes them through a hierarchical architecture to calculate SEDs. The model comprises three modules. The initial feature embedding module uses a 1D convolution layer (64 filters, 3 kernels, and ReLU activation) to capture local spectral features, and reshape the output into a 64×2982 tensor. The SE feature refinement module is then employed, in which a global average pooling (GAP) layer compresses global spatial information into a channel-wise descriptor. This descriptor is connected by two dense layers to fully capture channel-wise dependencies and compute channel-specific weights. These weights are then applied to the original feature map, producing the final weighted feature map. Finally, the SED regression module is used to flatten the refined features, pass them through a 64-neuron dense layer, and generate SEDs through an output layer.

The SENN model takes observed spectra as input features and their corresponding synthetic SEDs as training labels. Through training processes, SENN established a mapping relationship between observed spectra and synthetic SEDs, enabling it to calculate the synthetic SED associated with a given observed spectrum. With these synthetic SED and the observed magnitudes retrieved from the Spanish Virtual Observatory (SVO), we could calculate the masses, radii and luminosities of hot subdwarf stars reported in Culpan et al. (2022), if their atmospheric parameters are known (e.g., $T_{\rm eff}$ and $\log g$. see Section 2.3).

2.2. Training dataset

In previous studies (Lei et al. 2018, 2019, 2020, 2023a), 950 single-lined hot subdwarf stars were identified with LAMOST spectra. Their atmospheric parameters, i.e., effective temperature ($T_{\rm eff}$), surface gravity ($\log g$), and logarithmic number ratio of helium to hydrogen ($\log(n_{\rm He}/n_{\rm H})$), were determined by fitting H and He profiles with synthetic spectra. The synthetic spectra and SEDs of these stars were generated using `Synspec` (version 49; Lanz & Hubeny 2007) with nonlocal thermodynamic

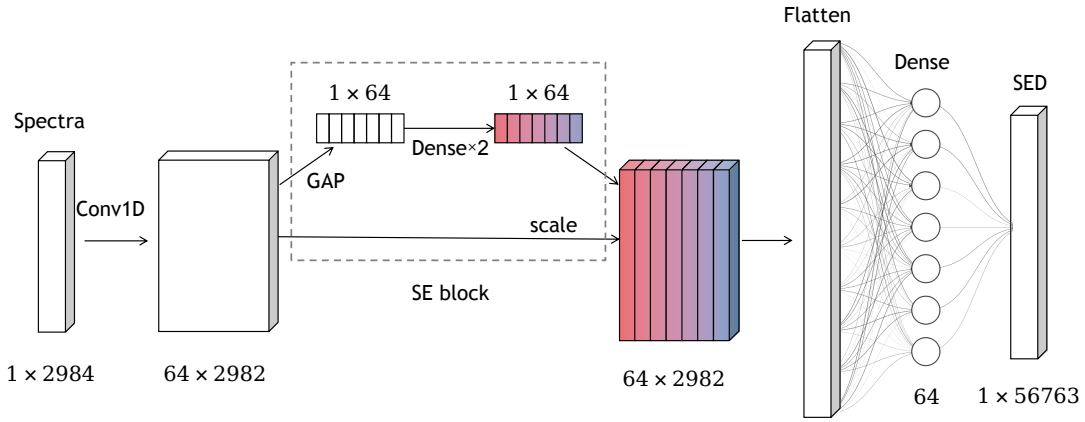

Fig. 1. Structure of deep learning model SENN. See Section 2.1 for detailed description.

equilibrium (NLTE) Tlusty atmospheres (version 204; Hubeny & Lanz 2017). See Lei et al. (2018) and Nemeth et al. (2014) for more details about the synthetic spectra and SED calculation.

In this study, the synthetic SEDs of the 950 stars mentioned above were used as a training sample for the SENN model, while the observed spectra of these stars were adopted as SENN inputs. The selected stars were split into two subsets, with 80% allocated to the training dataset and the remaining 20% reserved for the test dataset.

2.3. Known hot subdwarfs and their spectra

Culpan et al. (2022) compiled a catalog of the known hot subdwarf stars that contains 6616 unique sources collected from the literature. This catalog provides atmospheric parameters for 3087 stars and radial velocities for 2791 stars. To obtain the observed spectra for these stars, we cross-matched the catalog with the dataset of LAMOST DR11 and SDSS DR18, and then totally obtained 4289 spectra. After removing duplicated sources and low-quality spectra (e.g., that had a signal-to-noise ratio in the u band of less than 5.0), 3411 unique spectra of known hot subdwarfs were left. Since $T_{\rm eff}$ and log g are necessary parameters to determine stellar masses and luminosities in this study, only stars with the two parameters reported in the catalog of Culpan et al. (2022) were finally selected for the following analysis, and it contains 2047 hot subdwarf stars.

Within the catalog of Culpan et al. (2022), the atmospheric parameters of hot subdwarfs were collected from different studies; these were predominantly derived through spectral fitting. However, as we lack the specific atmospheric models and parameters used in these works to calculate synthetic spectra for hot subdwarf stars, we did not employ the conventional method of deriving the SEDs for this selected sample with known atmospheric parameters. Instead, we utilized the highly efficient SENN model to compute the SEDs for these hot subdwarfs with corresponding observed spectra.

Using the SENN model constructed in Section 2.1 and the training dataset selected in Section 2.2, synthetic SEDs for 2047 selected hot subdwarf stars were calculated; these were then used to obtain stellar masses, radii, and luminosities, as is described in the next section. Note that the SENN model is much more efficient at calculating synthetic SEDs than traditional methods. For example, it just needs tens of seconds to obtain synthetic SEDs for 2000 stars, and would be more powerful when confronting with huge numbers of stars.

In Fig. 2, we compare the synthetic SED of a hot subdwarf star calculated using the SENN model (dashed blue curve) with that computed directly from the Tlusty model (solid red curve). The near-identical agreement between the two SEDs fully demonstrates that utilizing the deep learning method to calculate theoretical SEDs for hot subdwarfs is both feasible and reliable.

2.4. Determination of masses, radii, and luminosities for selected hot subdwarf stars

Using the synthetic SEDs calculated by SENN model, we obtained the flux density at the stellar surface within specific pass-bands. The synthetic flux density can be compared with the flux density observed on the Earth to determine the stellar angular diameters. The synthetic flux density at stellar surface, observed flux density on the Earth, stellar angular diameter, radius, and distance of the star have the following relationships (Heber et al. 2018; Lei et al. 2023b):

$$\frac{f(\lambda)}{F(\lambda)} = \frac{\theta^2}{4} = \frac{R^2}{d^2}, \tag{1}$$

where $f(\lambda)$ is the flux density observed on the Earth, $F(\lambda)$ is the synthetic flux density at stellar surface, θ is the angular diameter of the star, R is the radius of the star, and d is the stellar distance from the Earth.

If the distance of a star is known, the stellar radius can be determined according to Equation (1). Then, with the help of atmospheric parameters (e.g., log g and $T_{\rm eff}$), we can obtain the mass and luminosity of the star using the following equations:

$$M = \frac{gR^2}{G} \tag{2}$$

$$\frac{L}{L_\odot} = \left(\frac{R}{R_\odot}\right)^2 \left(\frac{T_{\rm eff}}{T_\odot}\right)^4, \tag{3}$$

where $L_\odot$, $R_\odot$, and $T_\odot$ are the luminosity, radius, and effective temperature of the Sun, respectively.

Distances for the stars selected in this study were calculated using Gaia DR3 parallaxes (Gaia Collaboration 2023) after zero-point correction (Lindegren et al. 2021). The flux density observed on the Earth were obtained by searching for photometric data using VO SED Analyzer (VOSA, Bayo et al. 2008) of SVO and converting observed magnitudes into fluxes.

When converting the observed magnitude into the corresponding observed flux on the Earth, an extinction correction

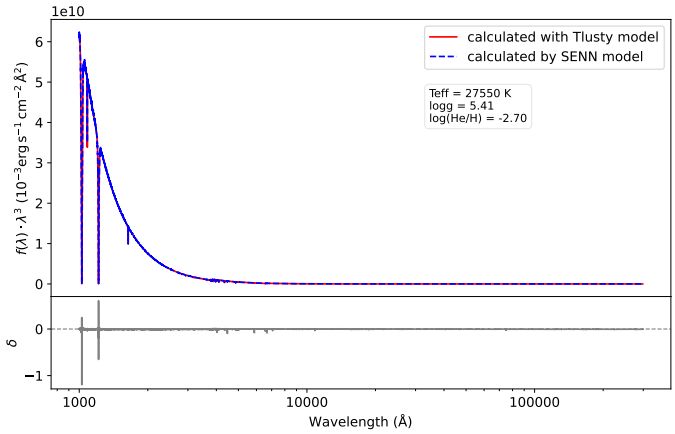

Fig. 2. Comparison between the synthetic SED calculated with Tlusty model (solid red curve) and the SED calculated by SENN model (dashed blue curve). The bottom panel displays the residual differences between the two SEDs.

must be applied. To determine the visual extinction, A_V, we fit the synthetic SEDs with the observed fluxes by treating A_V as a free parameter. For each trial value of A_V, the wavelength-dependent extinction, A_λ, was computed as

$$A_\lambda = A_V \times (k_\lambda/k_V), \tag{4}$$

where k_λ/k_V represents the normalized extinction law. The functional form of k_λ/k_V was adopted from Fitzpatrick (1999) with $R_V = 3.1$ and $k_V = 211.4$. The observed fluxes, $f_{obs}(\lambda)$, were then dereddened using

$$f(\lambda) = f_{obs}(\lambda) \times 10^{A_\lambda/2.5}, \tag{5}$$

which yielding the intrinsic flux density, $f(\lambda)$. The best-fit A_V were determined simultaneously through χ^2 minimization between the dereddened fluxes and the synthetic SEDs.

Using the method described above, we obtained masses, radii, and luminosities for the selected 2047 hot subdwarf stars. The stars with mass values lower than 0.1 $M_\odot$ or higher than 1.0 $M_\odot$ are not reported here, since these values could be significantly influenced by large uncertainties of input parameters, and are not reasonable for normal hot subdwarf stars. Furthermore, only stars with reliable parallaxes (e.g., $\sigma_\varpi/\varpi \leq 0.2$) are included in the following analysis. Thus, we finally have 1012 hot subdwarf stars for which the main parameters are reported in this study (see Table A.1), consisting of 606 sdB, 64 sdO, 206 sdOB, 9 He-sdB, 66 He-sdO, and 61 He-sdOB stars, respectively. The obtained parameter values are presented in Table A.1.

Using Monte Carlo methods, we obtained the statistical errors (σ_{sta}) for mass, radius, and luminosity of the selected stars. Specifically, we calculated the median values for the three parameters, along with their values at the 16th and 84th percentiles. This defines a 68% confidence interval around the median values and provides the corresponding asymmetric uncertainties.

On the other hand, we cross-matched the sample from this work with the sample from Schaffenroth et al. (2022), and identified 24 common sources. By comparing the masses, radii, and luminosities for these 24 sources, we determined the systematic errors (σ_{sys}), which were calculated using the following formula:

$$\sigma_{sys} = \frac{\sum(x_i - y_i)}{N},$$

where x_i is the parameter value calculated in this work, y_i is the parameter value calculated in Schaffenroth et al. (2022), and N is the number of common sources. The final errors (σ) was then calculated as

$$\sigma = \sqrt{\sigma_{sta}^2 + \sigma_{sys}^2}. \tag{6}$$

Using the method described above, we obtained systematic errors of 0.02 $M_\odot$, 0.002 $R_\odot$, and 1.4 $L_\odot$ for mass, radius and luminosity, respectively. In Table A.1, we presented the final errors for these three parameters, incorporating both statistical errors and systematic errors.

3. Results

3.1. Main parameters for selected hot subdwarf stars

The masses, radii, luminosities, and other important parameters for the 1012 selected hot subdwarf stars are presented in Table A.1. From left to right, it gives object names, Gaia source_id, spectral classification, T_{eff}, log g, extinction coefficient (A_V), Gaia parallax after zero-point correction, and four parameters obtained in this study, i.e., angular diameter, radius, luminosity, and mass. Of these stars, 601 have had their masses reported in previous studies. This means that the masses of 411 hot subdwarfs are reported for the first time in this study.

The four panels in Fig. 3 present the relationships between obtained masses and atmospheric parameters; for example, from top left to bottom right, it gives planes of mass versus T_{eff}, log g, log(n_{He}/n_H), and log L, respectively. It can be observed that most of the selected hot subdwarfs have radii of between 0.1 and 0.3 $R_\odot$, luminosities between 0.5 and 2.5 $L_\odot$, and masses between 0.2 and 0.8 $M_\odot$, respectively. These results are consistent with those of Lei et al. (2023b); see also Fig. 3 in their study.

3.2. Comparison with previous study

In order to evaluate the reliability of the masses, radii, and luminosities obtained in this study, we cross-matched the selected hot subdwarfs with the stars analyzed in Schaffenroth et al. (2022) and Lei et al. (2023b), respectively. Comparisons of masses, radii, and luminosities for the common stars are shown in the panels of Fig. 4. As can be seen in the figure, there is a notable agreement between the results of the present study and previous research, particularly with respect to radius and luminosity. However, the comparison of mass exhibits a slightly larger dispersion than the other two parameters. This is mainly due to the fact that the large uncertainties of surface gravity would directly influence stellar mass determination (see Equation 2), while it is not used in the determination of radius and luminosity (see Equations 1 and 3).

3.3. Mass distribution of hot subdwarf stars

Since the precision of masses obtained in this study depends mainly on the precision of the parallax (i.e., distance) and surface gravity, we show the mass distribution with different uncertainties of parallax and surface gravity in Fig. 5. In the left panel, the entire sample has been split into three groups according to the relative parallax uncertainty (e.g., $\sigma_\varpi/\varpi \leq 0.2$, 0.1 and 0.05, respectively). As expected, with the parallax precision increasing from 0.2 to 0.05, the number of hot subdwarf stars in each mass bin decreases. However, the three groups of hot subdwarfs show very similar mass distributions. As can be seen, all groups have

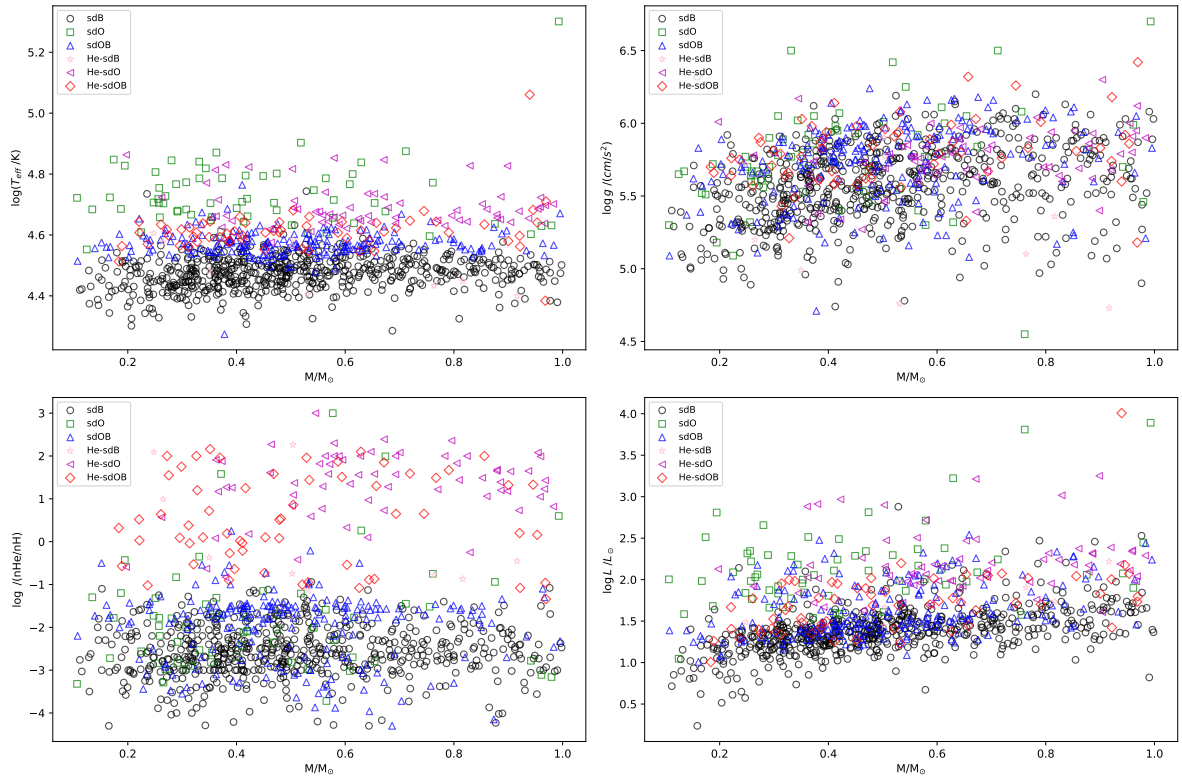

Fig. 3. Relationship between mass and atmospheric parameters for the selected hot subdwarfs. Labels with different colors indicate the spectral classification from Culpan et al. (2022).

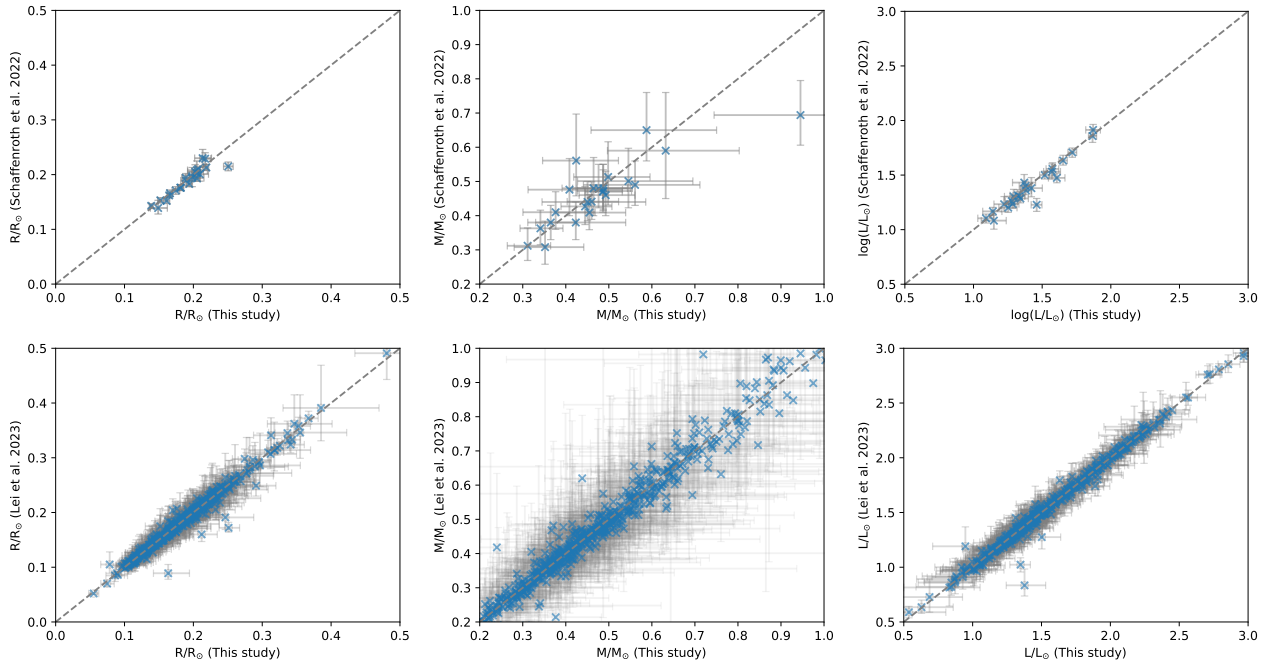

Fig. 4. Top panels: Comparison of radii, masses, and luminosities between this study and Schaffenroth et al. (2022). Bottom panels: Comparison of radii, masses, and luminosities between this study and Lei et al. (2023b).

a wide mass range of 0.1−1.0 $M_\odot$ and present two distinct peaks: a primary peak at 0.47 $M_\odot$ and a secondary peak at 0.37 $M_\odot$ (see detailed discussion on the mass distribution in Section 4). On the other hand, the entire sample has been separated into three other groups in the right panel according to the relative uncertainty of surface gravity (e.g., uncertainty of log g over log g less than 0.09, 0.02, and 0.007, respectively). The three groups in this panel show very similar mass distributions to those in the left panel, which also present two distinct peaks at the same mass values. Considering similar mass distributions for different precisions of parameters, all the selected hot subdwarf stars were adopted in the following analysis.

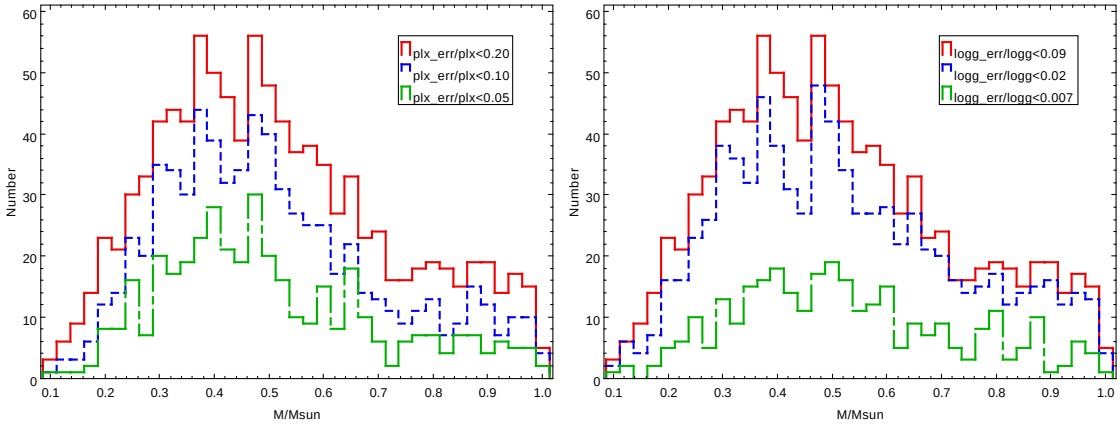

Fig. 5. Mass distribution for selected hot subdwarfs with different precisions of parallax (left panel) and surface gravity (right panel). See main text for details.

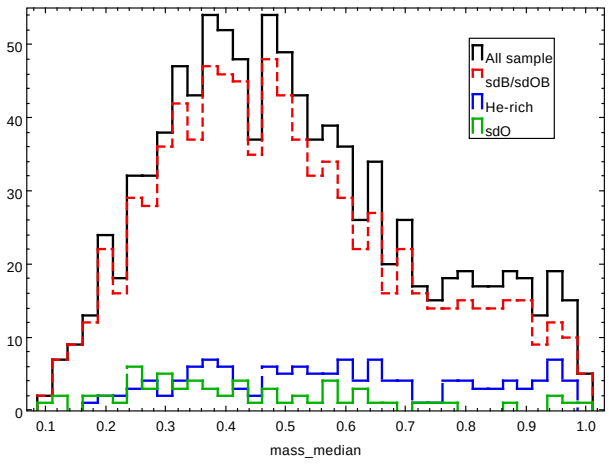

Fig. 6. Mass distributions for selected hot subdwarf stars with different spectral classifications.

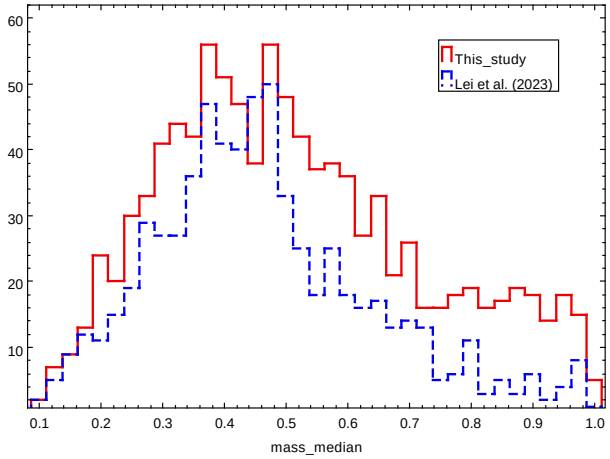

Fig. 7. Comparison of mass distribution between this study (red histogram) and Lei et al. (2023b) (dashed blue histogram).

In Fig. 6, we present the mass distributions for hot subdwarf stars according to their spectral classifications; for example, He-poor sdB/sdOB (dashed red histogram), He-rich stars (blue histogram, including He-sdB, He-sdO, and He-sdOB), and He-poor sdO (green histogram). The mass distribution of He-poor sdB/sdOB stars, which make up the majority of the hot subdwarf population, closely mirrors that of the entire sample, with two peaks at 0.47 and 0.37 $M_\odot$. For He-rich hot subdwarfs, two peaks are also present, but the values differ from those seen in sdB/sdOB, occurring at 0.4 and 0.58 $M_\odot$ (see the discussion in Section 4.3), respectively. However, He-poor sdO stars have a much flatter mass distribution and consist primarily of low-mass stars.

4. Discussion

4.1. Comparison of mass distribution with previous study

We compared the mass distribution of the entire sample with that of Lei et al. (2023b) in Fig. 7. Both mass distributions exhibit a wide mass range of 0.1−1.0 $M_\odot$. This is likely due to the large uncertainties of the input parameters (e.g., parallax and surface gravity) that were used in both studies to estimate the mass of hot subdwarf stars. In general, the two mass distributions show a basic consistency in that a primary peak appears around 0.47 $M_\odot$, and the distribution trend for the low-mass and high-mass sides is nearly the same. As is described in Section 3.3, in addition to the primary one, a second mass peak (around 0.37 $M_\odot$) is also clearly presented in the mass distribution of this study (red histogram). Nevertheless, this distinct feature is much more obscure in the mass distribution of Lei et al. (2023b) (dashed blue histogram). Note that the input surface gravities used to calculate mass for the two studies are from different catalogs. The parameters used in this study are from the catalog of Culpan et al. (2022), which were collected from other literature (Geier 2020; Luo et al. 2021; Jeffery et al. 2021). While the parameters used in Lei et al. (2023b) are from Lei et al. (2018, 2019, 2020, 2023a). The method of spectral analysis and the observed spectra used in these studies could be different, which would lead to the differences in obtained parameters. For example, the systematic errors of surface gravity between Luo et al. (2021) and Lei et al. are around 0.07 dex. Thus, these differences would cause an inconsistency in the mass distribution, especially for some local features.

4.2. Mass distribution of He-poor sdB/sdOB stars

Han et al. (2003) (hereafter Han03) have carried out a detailed BPS study on the formation of sdB-type hot subdwarfs. In their study, 12 sets of models were constructed with various input

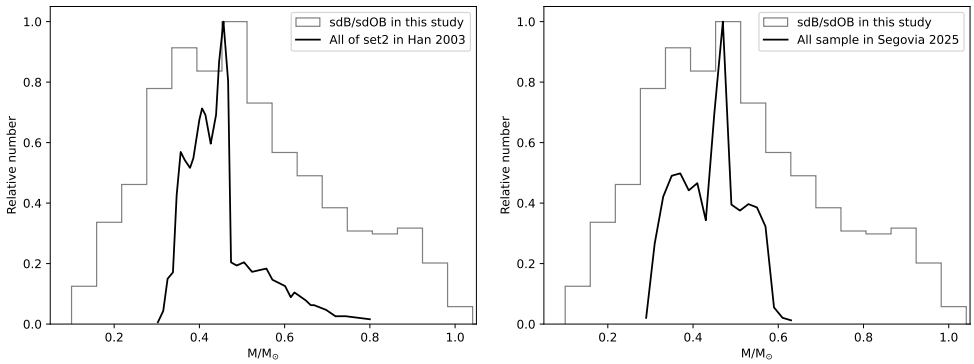

Fig. 8. Left panel: Comparison of mass distribution for sdB/sdOB stars between this study (gray histogram) and Han03 (solid black curve). Right panel: Comparison of mass distribution for sdB/sdOB stars between this study (gray histogram) and Rodríguez-Segovia et al. (2025) (solid black curve).

parameters to investigate their impacts on the formation of sdB stars. Among these models, the model of set 2 (with $Z = 0.02$, a flat initial mass ratio distribution, $q_{\rm crit} = 1.5$, $\alpha_{\rm CE} = \alpha_{\rm th} = 0.75$) was chosen as the best-fitting model in their study, capable of satisfying most of the observed properties for sdB stars. These results from BPS models are highly convenient for making direct comparisons with observations.

The left panel of Fig. 8 exhibits comparisons between the mass distribution of set 2 in Han03 (solid black curve) and that of this study (gray histogram). As is discussed in Section 4.1, the mass distribution of sdB/sdOB stars in this study shows a wide range from 0.1 to 1.0 $M_\odot$ due to the large uncertainties of the surface gravity and parallax, while the mass distribution of Han03 ranges from 0.3 to 0.8 $M_\odot$, which is narrower than that of this study. Since the minimum core mass for He ignition is about 0.3 $M_\odot$ (see Tables 1 and 2 in Han et al. 2002), there is a cutoff of mass around 0.3 $M_\odot$ for the low-mass side in the distribution of Han03. Therefore, the stars with masses of less than 0.3 $M_\odot$ in this study could be low-mass WDs or extremely low-mass (ELM) WDs (also see the discussion in Section 4.4 of Lei et al. 2023b).

Furthermore, three distinct peaks are presented in the mass distribution of Han03, at around 0.46, 0.4, and 0.36 $M_\odot$. These were generated through the combination of the first CE, the second CE, and the first stable RLOF channels (see Fig. 12 and Section 7.3 in their study). As can clearly be seen in the panel, the primary mass peak (around 0.47 $M_\odot$) in our study is consistent very well with the model prediction of Han03. The secondary mass peak in our study (e.g., around 0.36 $M_\odot$) corresponds to the left mass peak in Han03, which demonstrates that these stars are mainly produced by the stable RLOF channel with their progenitors at the Hertzsprung gap evolution stage. On the other hand, the middle mass peak (e.g., around 0.4 $M_\odot$) in Han03 is obscure in our mass distribution, for which the stars are mainly produced from the first and the second CE channel with the mass of progenitors around 1.9 $M_\odot$ (see Table 1 in Han et al. 2002).

Rodríguez-Segovia et al. (2025) also studied the impacts of various parameters on the formation of sdB stars through BPS methods. Unlike previous BPS models (e.g., Han03, Clausen et al. 2012), they considered H-rich shells using an analytic prescription in the study that gets more closer to the real evolution of sdB stars. In the right panel of Fig. 8, we compare the mass distribution predicted by Rodríguez-Segovia et al. (2025) with that of this study. The mass range of sdB stars predicted by Rodríguez-Segovia et al. (2025) (shown by the solid black curve in the right panel) is roughly from 0.3 to 0.62 $M_\odot$ and is a little narrower than that of Han03 and this study. Note that the results of two He-WDs merging are not included in the BPS code COMPAS (Riley et al. 2022) that was used in their study[1]; therefore, some massive hot subdwarf stars are absent in the mass distribution of Rodríguez-Segovia et al. (2025). As is shown in the panel, a sharp primary peak around 0.47 $M_\odot$ is clearly presented in both two mass distributions, which indicates a good agreement between the predictions of BPS model and observations. Furthermore, a second peak of around 0.37 $M_\odot$ is also presented in the mass distribution of Rodríguez-Segovia et al. (2025) (see also Fig. 7 in Rodríguez-Segovia & Ruiter 2025). Although the relative number of stars around this peak in their study is less than that of present study, it shows a one-to-one correspondence between the two studies.

4.3. Mass distribution for He-rich Hot subdwarfs

Two He-WDs merger is considered as the dominant formation channel for He-rich hot subdwarf stars (e.g., $\log(n{\rm He}/n{\rm H}) > -1.0$). The mass range of He-rich hot subdwarfs produced by this channel in Han03 is roughly from 0.42 to 0.76 $M_\odot$, with a relatively flat peak between 0.5 and 0.6 $M_\odot$. Zhang & Jeffery (2012) studied three different merging models for two He-WDs, and found that the results could explain most of observed gravities, effective temperatures, and surface chemical abundance for He-rich stars. Furthermore, Zhang et al. (2017) found that the mergers of He-WDs with low-mass MS stars could contribute to the formation of intermediate He-rich (iHe-rich) hot subdwarfs. On the other hand, Meng & Luo (2021) proposed that MS companions could survive Ia SN explosions and evolve as He-rich hot subdwarfs (see also Ji et al. 2024). They obtained a wide mass range of 0.35 to 1.0 $M_\odot$ for this formation channel, with a mass peak at around 0.4 $M_\odot$.

As was mentioned above, Lei et al. (2023b) obtained a wide mass range and a sharp mass peak around 0.42 $M_\odot$ for He-rich hot subdwarf stars observed by LAMOST. The mass peak in their study is much lower than the prediction of Han03 and Zhang & Jeffery (2012). On the other hand, the mass peak in Lei et al. (2023b) is basically consistent with the value predicted by Meng & Luo (2021), but the birth rate for this

[1] Although the results of two He-WDs merging are not taken into account in COMPAS, Rodríguez-Segovia et al. (2025) still give a simplified and qualitative analysis on this channel; see Section 3.2.4 in their study and Section 4.3 in this study for details.

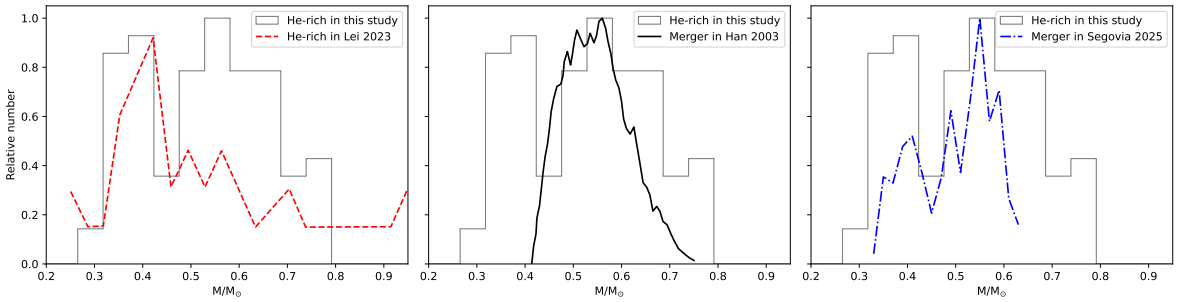

Fig. 9. Left panel: Comparison of mass distribution for He-rich stars between this study (gray histogram) and Lei et al. (2023b) (dotted red curve). Middle panel: Comparison of mass distribution for He-rich stars between this study and Han03 (solid black curve). Right panel: Comparison of mass distribution for He-rich stars between this study and Rodríguez-Segovia et al. (2025) (dash-dotted blue curve).

channel could be too low to explain the discovered He-rich hot subdwarfs (see Section 4.1 of Meng & Luo 2021). According to these results, Lei et al. (2023b) proposed that, besides the two He-WDs merger, some other channels could contribute to the formation of He-rich hot subdwarfs. Luo et al. (2024) came to a similar conclusion after analyzing the surface chemical abundances of He-rich hot subdwarf stars.

However, only 39 He-rich stars in group 3 of their sample (see Table 2 in Lei et al. 2023b), this sample limitation and incompleteness would influence the statistical results for mass distribution. Thanks to the deep learning model SENN designed in the present study (see Section 2.1), more than 2000 synthetic SEDs of the selected hot subdwarfs were calculated. Using these information, the masses of 131 He-rich stars were determined in this study, with the sample size being much larger than that analyzed in Lei et al. (2023b). Therefore, a comparison of the mass distribution between this study and previous studies could help us better understand the formation of He-rich hot subdwarf stars.

In the left panel of Fig. 9, we compare the mass distribution of He-rich stars obtained in the present study with that of in Lei et al. (2023b). As can be seen in the panel, it exhibits a relatively wide mass distribution that is roughly from 0.3 to 0.9 $M_\odot$ for both two studies (Note that hot subdwarf stars with masses of less than 0.3 $M_\odot$ cannot be produced in model predictions; thus, we excluded these stars from our results for the comparison). Two distinct mass peaks are presented in the mass distribution of this study (gray histogram): a primary peak around 0.56 $M_\odot$ and a secondary peak around 0.4 $M_\odot$. As was mentioned above, a sharp mass peak around 0.42 $M_\odot$ is clearly shown in the mass distribution of Lei et al. (2023b) (dotted red curve), which corresponds to the secondary mass peak in this study. However, it could be due to the small sample size used in the study of Lei et al. (2023b) that no distinct mass peak between 0.5 and 0.6 $M_\odot$ can be distinguished in their mass distribution.

In the middle panel of Fig. 9, we compare the mass distribution of He-rich stars in this study with that of Han03. As can be seen clearly in the panel, our mass distribution is much wider than that in Han03 (e.g., roughly from 0.42 to 0.76 $M_\odot$, solid black curve). As was discussed in Section 4.1, this could be due to the large uncertainties of the parallax and gravity, which significantly affect the precision of mass determination in this study. He-rich stars produced through two He-WDs merger in Han03 present a flat mass peak between 0.5 and 0.6 $M_\odot$, which could corresponding roughly to the primary mass peak around 0.56 $M_\odot$ in this study. However, the secondary mass peak around 0.4 $M_\odot$ is not predicted by BPS models of Han03, which would demonstrate that two He-WDs merging channel cannot explain the formation of all He-rich hot subdwarf stars.

Nevertheless, when comparing our results with recent BPS model predictions from Rodríguez-Segovia et al. (2025), we arrive at a slightly different conclusion (see the right panel in Fig. 9). The mass distribution of He-rich stars from the merging channel of Rodríguez-Segovia et al. (2025) (dash-dotted blue curve) presents two distinct mass peaks around 0.55 $M_\odot$ and 0.41 $M_\odot$ (see Fig. 14 in their study), which correspond perfectly to the two peaks shown in our study (gray histogram). However, the relative number of He-rich stars around the secondary mass peak (e.g., 0.41 $M_\odot$) predicted by Rodríguez-Segovia et al. (2025) is less than in this study. As is discussed in Section 3.2.4 of their study, the secondary mass peak heavily depends on mass-transfer accretion efficiency at stable RLOF phase. It would disappear when the accretion efficiency equals 0, and it would merge with the primary peak and form a symmetrical distribution with a peak around 0.47 $M_\odot$ if the accretion efficiency equals 1.

Note that the formation of two He-WD binaries[2] requires two RLOF phases. The whole envelope of the primary star will be removed through stable mass transfer during the first RLOF phase, while the two components will be surrounded by a CE formed due to unstable mass transfer during the second RLOF phase, and the CE should be ejected before the two He-WDs binary is formed (Webbink 1984). The mass-transfer accretion efficiency during the first RLOF phase has significant effects on the loss of angular momentum due to mass loss from the system, which in turn determines the subsequent evolution of the orbital separation. Therefore, a lower accretion efficiency during the first RLOF phase would result in either systems not triggering CE events (too far from each other) or merging (too close), both resulting in a final configuration different from the two He-WD binaries.

Based on the discussion mentioned above, if the second mass peak (around 0.4 $M_\odot$) is a real feature, the two He-WDs merging channel could produce most of the observed He-rich hot subdwarf stars on the condition that mass transfer during the first RLOF phase to produce the two He-WDs' binary should be partially conserved, and the accretion efficiency is not too low.

5. Summary

In this study, a deep learning model SENN was designed to calculate synthetic SEDs for a large number of known hot sub-

[2] In Rodríguez-Segovia et al. (2025), the treatment of the two He-WDs' merging channel was very sample. They did not evolve the two He-WDs binary into merging phase, but instead considered the binary system as hot subdwarfs if they could merge within the age of our Universe (e.g., 14 Gyr).

dwarfs with the help of spectra from LAMOST and SDSS. Through the VOSA service of the Spanish Virtual Observatory, the physical parameters (e.g., masses, radii, and luminosities) of 1012 hot subdwarfs were obtained by comparing the synthetic SEDs with the observed flux density. With the obtained parameters for a large sample size, comparisons between observations and model predictions would help us understand the formation of hot subdwarf stars more deeply and comprehensively.

The two mass peaks (e.g., 0.47 and 0.37) in the mass distribution of sdB/sdOB stars are consistent with the prediction from BPS models, which corresponds to the production of CE ejection and stable RLOF respectively. There is also a primary peak (around 0.56 $M_\odot$) and a secondary peak (around 0.4 $M_\odot$) clearly visible in the mass distribution of He-rich stars. Although the primary mass peak is well predicted by BPS models, the occurrence of the secondary peak in the models depends heavily on the mass-transfer accretion efficiency at stable RLOF stage in binary evolution. These results indicate that the two He-WDs' merging channel could produce most of the observed He-rich hot subdwarf stars, but mass transfer should be partially conserved during the stable RLOF phase. Considering the large uncertainties of the masses obtained in this study, other alternative formation channels for He-rich hot subdwarfs would not be completely excluded. More accurate determinations of the physical parameters of hot subdwarf stars are urgently needed.

It is important to note that although we could efficiently obtain synthetic SEDs of hot subdwarfs using the SENN model, deriving their masses, radii, and luminosities still requires atmospheric parameters ($T_{\rm eff}$ and $\log g$). Accurate atmospheric parameters, however, must still be acquired through the conventional method of synthetic spectral fitting. Fortunately, we are actively exploring the use of machine learning methods to predict the atmospheric parameters of hot subdwarfs (Lei et al. 2026). This approach, in the near future, should enable us to directly obtain both the atmospheric parameters and masses of hot subdwarfs using artificial intelligence techniques, without having to compute stellar atmosphere models.

Data availability

Table A.1 is available at the CDS via https://cdsarc.cds.unistra.fr/viz-bin/cat/J/A+A/709/A52

Acknowledgements. We greatly thank the referee for his/her valuable comments and useful suggestions, which help improve the manuscript significantly. We also thank Nicolás Rodríguez-Segovia for his detailed suggestions on the discussion of Section 4.3. This work acknowledges support from the National Natural Science Foundation of China (Nos. 12073020, 12588202 and 12273055), Scientific Research Fund of Hunan Provincial Education Department grant No. 20K124 and 23A0132, the Strategic Priority Research Program of Chinese Academy of Sciences, grant No. XDB1160301. K.H. acknowledges support from the Scientific Research Funds of Hunan Provincial Education Department (Nos. 22A0099 and 24A0101). This research has made use of the Spanish Virtual Observatory (https://svo.cab.inta-csic.es) project funded by MCIN/AEI/10.13039/501100011025/ through grant PID2020-112949GB-I00. Guoshoujing Telescope (the Large Sky Area Multi-Object Fiber Spectroscopic Telescope LAMOST) is a National Major Scientific Project built by the Chinese Academy of Sciences. Funding for the project has been provided by the National Development and Reform Commission. LAMOST is operated and managed by the National Astronomical Observatories, Chinese Academy of Sciences.

References

Ahumada, R., Allende Prieto, C., Almeida, A., et al. 2020, ApJS, 249, 3
Bayo, A., Rodrigo, C., Barrado Y Navascués, D., et al. 2008, A&A, 492, 277
Bu, Y., Zeng, J., Lei, Z., & Yi, Z. 2019, ApJ, 886, 128
Castellani, M., & Castellani, V. 1993, ApJ, 407, 649
Cheng, Z., Kong, X., Wu, T., et al. 2024, ApJS, 274, 2
Clausen, D., Wade, R. A., Kopparapu, R. K., & O'Shaughnessy, R. 2012, ApJ, 746, 186
Copperwheat, C. M., Morales-Rueda, L., Marsh, T. R., Maxted, P. F. L., & Heber, U. 2011, MNRAS, 415, 1381
Cui, X.-Q., Zhao, Y.-H., Chu, Y.-Q., et al. 2012, RAA, 12, 1197
Culpan, R., Geier, S., Reindl, N., et al. 2022, A&A, 662, A40
Drilling, J. S., Jeffery, C. S., Heber, U., Moehler, S., & Napiwotzki, R. 2013, A&A, 551, A31
Fitzpatrick, E. L. 1999, PASP, 111, 63
Fontaine, G., Brassard, P., Charpinet, S., et al. 2012, A&A, 539, A12
Gaia Collaboration (Brown, A. G. A., et al.) 2021, A&A, 649, A1
Gaia Collaboration (Vallenari, A., et al.) 2023, A&A, 674, A1
Geier, S. 2020, A&A, 635, A193
Geier, S., Østensen, R. H., Nemeth, P., et al. 2017a, A&A, 600, A50
Geier, S., Østensen, R. H., Nemeth, P., et al. 2017b, Open Astron., 26, 164
Geier, S., Raddi, R., Gentile Fusillo, N. P., & Marsh, T. R. 2019, A&A, 621, A38
Han, Z., Podsiadlowski, P., Maxted, P. F. L., Marsh, T. R., & Ivanova, N. 2002, MNRAS, 336, 449
Han, Z., Podsiadlowski, P., Maxted, P. F. L., & Marsh, T. R. 2003, MNRAS, 341, 669
He, R., Meng, X., Lei, Z., Yan, H., & Lan, S. 2025, A&A, 693, A121
Heber, U. 1986, A&A, 155, 33
Heber, U. 2009, ARA&A, 47, 211
Heber, U. 2016, PASP, 128, 082001
Heber, U., Irrgang, A., & Schaffenroth, J. 2018, Open Astron., 27, 35
Howell, S. B., Sobeck, C., Haas, M., et al. 2014, PASP, 126, 398
Hubeny, I., & Lanz, T. 2017, ArXiv e-prints [arXiv:1706.01859]
Jeffery, C. S., Miszalski, B., & Snowdon, E. 2021, MNRAS, 501, 623
Ji, R.-J., Meng, X.-C., & Liu, Z.-W. 2024, RAA, 24, 055003
Kepler, S. O., Pelisoli, I., Koester, D., et al. 2019, MNRAS, 486, 2169
Lanz, T., & Hubeny, I. 2007, ApJS, 169, 83
Lei, Z., Zhao, J., Németh, P., & Zhao, G. 2018, ApJ, 868, 70
Lei, Z., Zhao, J., Németh, P., & Zhao, G. 2019, ApJ, 881, 135
Lei, Z., Zhao, J., Németh, P., & Zhao, G. 2020, ApJ, 889, 117
Lei, Z., He, R., Németh, P., et al. 2023a, ApJ, 942, 109
Lei, Z., He, R., Németh, P., et al. 2023b, ApJ, 953, 122
Lei, Z., Dong, Y., Kou, B., et al. 2026, ApJS, 283, 16
Li, J., Onken, C. A., Wolf, C., et al. 2022, MNRAS, 515, 3370
Li, Z., Zhang, Y., Chen, H., et al. 2024, ApJ, 964, 22
Lindegren, L., Bastian, U., Biermann, M., et al. 2021, A&A, 649, A4
Liu, W., Bu, Y., Kong, X., Yi, Z., & Liu, M. 2024, PASJ, 76, 329
Luo, Y., Németh, P., Deng, L., & Han, Z. 2019, ApJ, 881, 7
Luo, Y., Németh, P., Wang, K., Wang, X., & Han, Z. 2021, ApJS, 256, 28
Luo, Y., Németh, P., Wang, K., & Pan, Y. 2024, ApJS, 271, 21
Maxted, P. F. L., Heber, U., Marsh, T. R., & North, R. C. 2001, MNRAS, 326, 1391
Meng, X.-C., & Luo, Y.-P. 2021, MNRAS, 507, 4603
Miller Bertolami, M. M., Althaus, L. G., Unglaub, K., & Weiss, A. 2008, A&A, 491, 253
Miller Bertolami, M. M., Battich, T., Córsico, A. H., Althaus, L. G., & Wachlin, F. C. 2022, MNRAS, 511, L60
Moehler, S., Richtler, T., de Boer, K. S., Dettmar, R. J., & Heber, U. 1990, A&AS, 86, 53
Napiwotzki, R., Karl, C. A., Lisker, T., et al. 2004, Ap&SS, 291, 321
Nemeth, P., Östensen, R., Tremblay, P., & Hubeny, I. 2014, ASP Conf. Ser., 481, 95
Pelisoli, I., Vos, J., Geier, S., Schaffenroth, V., & Baran, A. S. 2020, A&A, 642, A180
Ricker, G. R., Winn, J. N., Vanderspek, R., et al. 2015, J. Astron. Telesc. Instrum. Syst., 1, 014003
Riley, J., Agrawal, P., Barrett, J. W., et al. 2022, ApJS, 258, 34
Rodríguez-Segovia, N., & Ruiter, A. J. 2025, MNRAS, 539, 3273
Rodríguez-Segovia, N., Ruiter, A. J., & Seitenzahl, I. R. 2025, PASA, 42, e012
Schaffenroth, V., Barlow, B. N., Geier, S., et al. 2019, A&A, 630, A80
Schaffenroth, V., Pelisoli, I., Barlow, B. N., Geier, S., & Kupfer, T. 2022, A&A, 666, A182
Schaffenroth, V., Barlow, B. N., Pelisoli, I., Geier, S., & Kupfer, T. 2023, A&A, 673, A90
Tan, L., Mei, Y., Liu, Z., et al. 2022, ApJS, 259, 5
Webbink, R. F. 1984, ApJ, 277, 355
Zhang, X., & Jeffery, C. S. 2012, MNRAS, 419, 452
Zhang, X., Hall, P. D., Jeffery, C. S., & Bi, S. 2017, ApJ, 835, 242
Zhao, G., Zhao, Y.-H., Chu, Y.-Q., Jing, Y.-P., & Deng, L.-C. 2012, RAA, 12, 723
Zou, X., & Lei, Z. 2024, PASJ, 76, 1084

Appendix A: Main parameters for the selected hot subdwarf stars

Table A.1. Main parameters for part of 1,012 selected hot subdwarf stars

Name	Source_id Gaia DR3	sp_class	$T_{\rm eff}$ K	log g (cm s^{-2})	$A_{\rm V}$ mag	plx_zp mas	Angular diameter log(rad)	Radius R/R$_\odot$	Luminosity L/L$_\odot$	Mass M/M$_\odot$
BD+423250	2105469320138052864	sdB	28700 ± 1000	5.08 ± 0.02	0.422	4.1508 ± 0.0319	$-10.268^{+0.036}_{-0.020}$	$0.287^{+0.003}_{-0.003}$	$50.2^{+7.5}_{-6.8}$	$0.36^{+0.03}_{-0.03}$
BD+481777	825628714431805056	sdO	47565 ± 251	5.84 ± 0.04	0.010	4.2560 ± 0.0617	$-10.503^{+0.019}_{-0.014}$	$0.163^{+0.003}_{-0.003}$	$122.7^{+4.7}_{-4.5}$	$0.67^{+0.07}_{-0.07}$
BD-32179	3068744791442939904	sdO	59121 ± 686	4.55 ± 0.03	0.010	1.0124 ± 0.0666	$-10.458^{+0.020}_{-0.029}$	$0.767^{+0.054}_{-0.047}$	$6445.7^{+992.0}_{-811.9}$	$0.76^{+0.13}_{-0.10}$
BPSCS22890-74	4420741294390728448	sdB	24560 ± 567	5.14 ± 0.06	1.135	1.0170 ± 0.0312	$-10.690^{+0.064}_{-0.016}$	$0.430^{+0.014}_{-0.013}$	$60.4^{+7.1}_{-6.4}$	$0.93^{+0.15}_{-0.13}$
Bal90100005	2845710850610464640	sdB	32789 ± 123	5.66 ± 0.02	0.302	1.2124 ± 0.0358	$-11.098^{+0.011}_{-0.052}$	$0.146^{+0.005}_{-0.005}$	$22.2^{+2.0}_{-1.9}$	$0.36^{+0.04}_{-0.03}$
Bal90900004	1874534323107953664	sdB	42860 ± 1590	5.51 ± 0.12	0.168	1.3991 ± 0.0553	$-10.883^{+0.018}_{-0.016}$	$0.207^{+0.009}_{-0.008}$	$129.9^{+23.4}_{-20.3}$	$0.51^{+0.17}_{-0.13}$
CBS250	1373881186687373696	sdB	32280 ± 140	5.76 ± 0.03	0.052	0.8909 ± 0.0328	$-11.194^{+0.010}_{-0.007}$	$0.159^{+0.006}_{-0.006}$	$24.6^{+2.4}_{-2.2}$	$0.53^{+0.06}_{-0.05}$
CBS274	1605239049014274560	sdOB	36833 ± 2000	5.83 ± 0.20	0.030	0.3374 ± 0.0601	$-11.708^{+0.014}_{-0.005}$	$0.128^{+0.028}_{-0.020}$	$27.3^{+15.3}_{-9.1}$	$0.41^{+0.34}_{-0.18}$
CBS282	1591755325606144640	sdOB	36728 ± 932	6.02 ± 0.14	0.457	0.3160 ± 0.0622	$-11.696^{+0.024}_{-0.010}$	$0.139^{+0.034}_{-0.023}$	$31.5^{+17.6}_{-9.9}$	$0.75^{+0.53}_{-0.29}$
CBS374	1471988375850922368	sdOB	35110 ± 73	6.08 ± 0.02	0.093	1.0166 ± 0.0376	$-11.195^{+0.025}_{-0.006}$	$0.139^{+0.006}_{-0.005}$	$26.3^{+2.5}_{-2.3}$	$0.85^{+0.08}_{-0.07}$
CBS98	810691780249660800	sdOB	33588 ± 147	5.39 ± 0.03	0.029	0.6313 ± 0.0665	$-11.408^{+0.015}_{-0.008}$	$0.136^{+0.016}_{-0.013}$	$21.0^{+5.4}_{-4.1}$	$0.16^{+0.05}_{-0.04}$
EGGR113	4422600328035803264	sdO	61075 ± 1182	5.77 ± 0.05	0.146	0.7145 ± 0.0416	$-11.398^{+0.005}_{-0.034}$	$0.124^{+0.008}_{-0.007}$	$192.9^{+29.2}_{-24.8}$	$0.33^{+0.06}_{-0.05}$
FBS0021+418	382086995098288896	sdB	29032 ± 477	5.12 ± 0.06	0.224	0.3996 ± 0.0475	$-11.341^{+0.013}_{-0.004}$	$0.252^{+0.034}_{-0.027}$	$40.7^{+12.1}_{-8.6}$	$0.31^{+0.10}_{-0.07}$
FBS0033+376	368263110278860544	sdB	38970 ± 1330	5.89 ± 0.10	0.076	1.4164 ± 0.0409	$-11.144^{+0.008}_{-0.006}$	$0.112^{+0.004}_{-0.004}$	$26.2^{+4.3}_{-3.9}$	$0.36^{+0.10}_{-0.08}$
FBS0051+377	364742852004132736	sdOB	35103 ± 116	5.91 ± 0.02	0.080	1.0341 ± 0.0418	$-11.181^{+0.018}_{-0.006}$	$0.142^{+0.006}_{-0.006}$	$27.3^{+2.8}_{-2.5}$	$0.59^{+0.06}_{-0.06}$
FBS0102+362	369576820516013824	sdB	32628 ± 98	5.68 ± 0.02	0.011	2.6839 ± 0.0523	$-10.729^{+0.007}_{-0.007}$	$0.154^{+0.004}_{-0.004}$	$24.1^{+1.7}_{-1.7}$	$0.41^{+0.03}_{-0.03}$
FBS0104+367	369621277722573568	sdB	31086 ± 120	5.94 ± 0.04	0.157	0.7730 ± 0.0421	$-11.236^{+0.044}_{-0.008}$	$0.166^{+0.010}_{-0.009}$	$23.0^{+3.1}_{-2.7}$	$0.87^{+0.14}_{-0.12}$
FBS0106+374	369573831218501376	sdB	30340 ± 218	5.75 ± 0.05	0.141	1.1993 ± 0.0391	$-10.953^{+0.005}_{-0.006}$	$0.207^{+0.007}_{-0.007}$	$32.6^{+2.8}_{-2.6}$	$0.88^{+0.13}_{-0.11}$
FBS0117+396	371711041304831616	sdB	28500 ± 100	5.42 ± 0.01	0.060	0.5853 ± 0.0462	$-11.279^{+0.035}_{-0.007}$	$0.198^{+0.017}_{-0.014}$	$23.3^{+4.4}_{-3.5}$	$0.38^{+0.07}_{-0.06}$
FBS0156+439	346721341030064640	He-sdOB	43970 ± 1190	5.72 ± 0.16	0.166	0.5015 ± 0.0491	$-11.401^{+0.031}_{-0.009}$	$0.176^{+0.019}_{-0.016}$	$103.6^{+26.9}_{-20.1}$	$0.59^{+0.31}_{-0.20}$
FBS0203+374	330722897089067392	sdB	28744 ± 303	5.47 ± 0.04	0.150	1.0701 ± 0.0367	$-10.984^{+0.044}_{-0.004}$	$0.214^{+0.008}_{-0.007}$	$28.0^{+2.7}_{-2.6}$	$0.49^{+0.06}_{-0.06}$
FBS0206+428	351633546665907200	sdB	25735 ± 251	5.14 ± 0.03	0.135	0.9280 ± 0.0366	$-11.019^{+0.006}_{-0.007}$	$0.229^{+0.009}_{-0.009}$	$20.6^{+2.4}_{-2.2}$	$0.26^{+0.04}_{-0.03}$
FBS0208+390	332606704106366848	sdB	38743 ± 269	6.15 ± 0.04	0.106	0.7313 ± 0.0419	$-11.439^{+0.008}_{-0.011}$	$0.111^{+0.007}_{-0.006}$	$24.8^{+3.5}_{-3.0}$	$0.63^{+0.10}_{-0.09}$
FBS0212+334	326009496898928896	sdB	29697 ± 197	5.63 ± 0.04	0.254	1.2116 ± 0.0350	$-10.875^{+0.012}_{-0.006}$	$0.243^{+0.007}_{-0.007}$	$41.3^{+3.0}_{-2.9}$	$0.92^{+0.11}_{-0.10}$
FBS0314+372	235323736345986176	sdB	29283 ± 192	5.42 ± 0.03	0.902	0.8740 ± 0.0403	$-11.085^{+0.007}_{-0.029}$	$0.209^{+0.010}_{-0.009}$	$28.8^{+3.3}_{-2.9}$	$0.42^{+0.06}_{-0.05}$
FBS0324+379	234861632224343424	sdB	24809 ± 298	5.27 ± 0.03	0.473	1.3008 ± 0.0340	$-10.908^{+0.009}_{-0.007}$	$0.210^{+0.006}_{-0.006}$	$15.0^{+1.8}_{-1.7}$	$0.30^{+0.03}_{-0.03}$
FBS0638+428	963881581386403072	sdB	28090 ± 161	5.29 ± 0.02	0.229	1.1992 ± 0.0344	$-10.985^{+0.042}_{-0.010}$	$0.191^{+0.006}_{-0.006}$	$20.4^{+1.9}_{-1.9}$	$0.26^{+0.03}_{-0.03}$
FBS0639+391	944892878136403712	sdB	29658 ± 509	5.53 ± 0.08	0.372	0.8262 ± 0.0358	$-11.070^{+0.008}_{-0.007}$	$0.229^{+0.010}_{-0.010}$	$36.3^{+4.5}_{-4.0}$	$0.65^{+0.15}_{-0.12}$
FBS0646+386	944390774983674496	sdB	33238 ± 190	5.63 ± 0.03	0.234	0.7018 ± 0.0473	$-11.323^{+0.020}_{-0.012}$	$0.150^{+0.011}_{-0.010}$	$24.6^{+3.9}_{-3.4}$	$0.35^{+0.06}_{-0.05}$
FBS1400+389	1495942160078351744	sdOB	18800 ± 1000	4.71 ± 0.10	0.029	1.4515 ± 0.0345	$-10.534^{+0.020}_{-0.045}$	$0.449^{+0.011}_{-0.011}$	$22.6^{+5.5}_{-4.7}$	$0.38^{+0.10}_{-0.08}$
FBS1531+381	1375814952762454272	sdB	29230 ± 125	5.58 ± 0.03	0.029	1.9294 ± 0.0345	$-10.805^{+0.013}_{-0.164}$	$0.181^{+0.004}_{-0.004}$	$21.5^{+1.7}_{-1.6}$	$0.46^{+0.04}_{-0.04}$
FBS1715+424	1360139937040515072	sdO	58438 ± 514	6.11 ± 0.03	0.010	2.3950 ± 0.0387	$-10.911^{+0.011}_{-0.009}$	$0.114^{+0.003}_{-0.003}$	$135.4^{+6.8}_{-6.4}$	$0.61^{+0.05}_{-0.05}$
FBS1745+437	1349088676950060672	sdB	33601 ± 109	5.56 ± 0.02	0.073	1.0659 ± 0.0262	$-11.132^{+0.008}_{-0.006}$	$0.153^{+0.004}_{-0.004}$	$26.9^{+2.0}_{-1.9}$	$0.31^{+0.03}_{-0.03}$
FBS2255+404	1930945626165804032	He-sdOB	48127 ± 277	5.92 ± 0.04	0.355	0.4056 ± 0.0444	$-11.490^{+0.049}_{-0.010}$	$0.176^{+0.022}_{-0.017}$	$149.9^{+39.4}_{-28.1}$	$0.95^{+0.27}_{-0.19}$
FBS2307+338	1911572540520290048	He-sdO	50664 ± 390	5.85 ± 0.04	0.219	0.4957 ± 0.0502	$-11.435^{+0.006}_{-0.011}$	$0.165^{+0.018}_{-0.015}$	$160.2^{+38.3}_{-28.2}$	$0.70^{+0.18}_{-0.14}$
FBS2347+385	2881551562420806784	sdB	23770 ± 350	5.38 ± 0.06	0.269	3.9390 ± 0.0341	$-10.434^{+0.026}_{-0.011}$	$0.207^{+0.003}_{-0.003}$	$12.3^{+1.6}_{-1.6}$	$0.37^{+0.06}_{-0.05}$
Feige114	1858674589447492608	sdOB	37689 ± 189	5.56 ± 0.02	0.148	1.2354 ± 0.0317	$-10.983^{+0.023}_{-0.006}$	$0.186^{+0.005}_{-0.005}$	$62.5^{+3.8}_{-3.6}$	$0.46^{+0.04}_{-0.04}$
Feige26	2503706418759709184	He-sdO	65608 ± 912	5.46 ± 0.04	0.010	0.5763 ± 0.0471	$-11.247^{+0.007}_{-0.010}$	$0.218^{+0.019}_{-0.017}$	$793.7^{+154.1}_{-121.7}$	$0.50^{+0.11}_{-0.09}$
Feige34	781164326766404736	sdO	62400 ± 330	5.95 ± 0.02	0.145	4.4105 ± 0.1039	$-10.645^{+0.069}_{-0.018}$	$0.113^{+0.003}_{-0.003}$	$174.4^{+9.3}_{-8.8}$	$0.42^{+0.04}_{-0.03}$
Feige67	3935488605023787392	sdO	61114 ± 318	5.92 ± 0.01	0.105	2.9833 ± 0.0735	$-10.739^{+0.010}_{-0.039}$	$0.136^{+0.004}_{-0.004}$	$232.9^{+13.0}_{-12.0}$	$0.56^{+0.04}_{-0.04}$
GALEXJ00468+1956	2801277176253968640	sdB	32891 ± 111	5.84 ± 0.02	0.200	0.9281 ± 0.0413	$-11.213^{+0.041}_{-0.008}$	$0.146^{+0.007}_{-0.006}$	$22.2^{+2.5}_{-2.3}$	$0.53^{+0.06}_{-0.05}$
GALEXJ00476+3123	360511037906831872	sdB	31069 ± 166	5.65 ± 0.03	0.207	1.0593 ± 0.0383	$-11.149^{+0.042}_{-0.011}$	$0.148^{+0.006}_{-0.006}$	$18.4^{+2.0}_{-1.9}$	$0.36^{+0.04}_{-0.04}$
GALEXJ00498+3522	363795760175504768	sdOB	36551 ± 243	5.74 ± 0.04	0.063	0.8767 ± 0.0412	$-11.251^{+0.010}_{-0.016}$	$0.142^{+0.007}_{-0.007}$	$32.5^{+3.7}_{-3.3}$	$0.41^{+0.06}_{-0.05}$
GALEXJ01012+3125	312628749626419328	sdB	28202 ± 155	5.45 ± 0.02	0.063	1.8070 ± 0.0362	$-10.788^{+0.010}_{-0.017}$	$0.201^{+0.005}_{-0.004}$	$22.9^{+1.8}_{-1.7}$	$0.41^{+0.03}_{-0.03}$
GALEXJ01194+4901	400211958948711552	He-sdOB	43720 ± 510	5.86 ± 0.21	0.313	1.2614 ± 0.0326	$-10.965^{+0.017}_{-0.012}$	$0.189^{+0.005}_{-0.005}$	$117.7^{+8.6}_{-8.0}$	$0.95^{+0.59}_{-0.37}$
GALEXJ01509+3107	304311150320629376	sdB	30183 ± 189	5.84 ± 0.04	0.130	1.3955 ± 0.0367	$-11.041^{+0.004}_{-0.008}$	$0.145^{+0.004}_{-0.004}$	$15.6^{+1.7}_{-1.7}$	$0.53^{+0.06}_{-0.06}$
GALEXJ01543+4905	357580873780641920	sdB	32100 ± 410	5.50 ± 0.32	0.452	1.7860 ± 0.0250	$-10.871^{+0.008}_{-0.008}$	$0.166^{+0.003}_{-0.003}$	$26.4^{+2.1}_{-2.1}$	$0.32^{+0.35}_{-0.17}$
GALEXJ02069+1438	77515058657678592	sdB	30310 ± 660	5.77 ± 0.06	0.132	2.2104 ± 0.0447	$-10.881^{+0.010}_{-0.028}$	$0.133^{+0.003}_{-0.003}$	$13.3^{+1.9}_{-1.9}$	$0.38^{+0.06}_{-0.05}$
GALEXJ02163+2759	107585292928397568	sdB	25480 ± 450	5.35 ± 0.05	0.155	1.5540 ± 0.0313	$-10.767^{+0.028}_{-0.013}$	$0.244^{+0.005}_{-0.005}$	$22.5^{+2.4}_{-2.3}$	$0.49^{+0.07}_{-0.06}$
GALEXJ02328+4411	341195058150383104	sdB	33260 ± 420	5.73 ± 0.10	0.237	1.2611 ± 0.0577	$-11.082^{+0.011}_{-0.007}$	$0.145^{+0.007}_{-0.007}$	$23.1^{+2.9}_{-2.7}$	$0.41^{+0.12}_{-0.09}$
GALEXJ04158+0154	3259060049366022400	sdBV	34773 ± 123	5.79 ± 0.02	0.359	1.5335 ± 0.0402	$-11.003^{+0.014}_{-0.006}$	$0.144^{+0.004}_{-0.004}$	$27.1^{+2.1}_{-2.0}$	$0.46^{+0.04}_{-0.04}$
GALEXJ04205+0120	3255780171819962496	He-sdO	46050 ± 910	5.97 ± 0.16	0.081	2.4658 ± 0.0620	$-10.816^{+0.012}_{-0.006}$	$0.137^{+0.004}_{-0.004}$	$76.2^{+7.5}_{-6.9}$	$0.64^{+0.29}_{-0.20}$
GALEXJ04593-0228	3225359193340812288	sdB	30613 ± 608	5.70 ± 0.12	0.062	1.1390 ± 0.0412	$-11.197^{+0.033}_{-0.008}$	$0.124^{+0.005}_{-0.005}$	$12.0^{+2.0}_{-1.9}$	$0.28^{+0.09}_{-0.07}$
GALEXJ05369+3955	190970433715259904	He-sdOB	38898 ± 169	5.79 ± 0.04	0.507	1.3436 ± 0.0332	$-11.007^{+0.006}_{-0.008}$	$0.164^{+0.005}_{-0.004}$	$55.1^{+3.3}_{-3.1}$	$0.60^{+0.07}_{-0.06}$
GALEXJ05557+6408	287018271958898560	sdO	45600 ± 3380	5.73 ± 0.39	0.462	1.9389 ± 0.0248	$-10.932^{+0.007}_{-0.023}$	$0.134^{+0.003}_{-0.003}$	$70.1^{+23.2}_{-18.7}$	$0.35^{+0.51}_{-0.21}$
GALEXJ06134+3420	3452237404778065152	sdOB	34250 ± 390	5.75 ± 0.10	0.432	1.7373 ± 0.0329	$-10.935^{+0.010}_{-0.010}$	$0.148^{+0.003}_{-0.003}$	$27.1^{+2.2}_{-2.1}$	$0.45^{+0.12}_{-0.10}$
GALEXJ063952.00+515658.00	992534888766785024	sdB	30400 ± 340	5.58 ± 0.13	0.065	3.0845 ± 0.0455	$-10.552^{+0.031}_{-0.006}$	$0.202^{+0.004}_{-0.004}$	$31.2^{+2.2}_{-2.1}$	$0.56^{+0.20}_{-0.15}$
GALEXJ06437+3201	937248901501446272	sdB	26956 ± 303	5.12 ± 0.04	0.331	1.0644 ± 0.0448	$-10.873^{+0.061}_{-0.008}$	$0.276^{+0.012}_{-0.011}$	$36.0^{+3.9}_{-3.5}$	$0.37^{+0.05}_{-0.05}$
GALEXJ06463+2920	3386622158606040960	sdOB	41489 ± 229	6.16 ± 0.03	0.073	2.1178 ± 0.0437	$-10.998^{+0.009}_{-0.016}$	$0.105^{+0.003}_{-0.003}$	$29.3^{+2.0}_{-1.9}$	$0.58^{+0.05}_{-0.05}$
GALEXJ07013+5329	981727582818800128	He-sdO	67230 ± 3880	5.60 ± 0.22	0.117	0.3925 ± 0.0431	$-11.375^{+0.012}_{-0.005}$	$0.238^{+0.029}_{-0.023}$	$1038.8^{+393.0}_{-282.0}$	$0.83^{+0.61}_{-0.35}$
GALEXJ07104+2333	3368383116127317120	sdB	55420 ± 24300	5.21 ± 0.43	0.724	0.5599 ± 0.0242	$-11.119^{+0.071}_{-0.016}$	$0.299^{+0.013}_{-0.013}$	$756.7^{+2464.1}_{-679.2}$	$0.53^{+0.90}_{-0.33}$
GALEXJ07108+5624	988436459174352512	sdB	39970 ± 980	5.91 ± 0.14	0.094	0.9733 ± 0.0521	$-11.251^{+0.009}_{-0.005}$	$0.128^{+0.007}_{-0.007}$	$37.5^{+6.1}_{-5.2}$	$0.49^{+0.20}_{-0.14}$
GALEXJ07248+1923	3362730178953977472	sdB	25777 ± 334	5.25 ± 0.03	0.172	0.9219 ± 0.0378	$-11.069^{+0.010}_{-0.006}$	$0.205^{+0.009}_{-0.008}$	$16.7^{+2.2}_{-2.1}$	$0.27^{+0.04}_{-0.04}$